



Electrocatalytic nitrate reduction to ammonia on defective Au₁Cu (111) single-atom alloys

Yuanzheng Zhang^a, Xiang Chen^a, Weilai Wang^a, Lifeng Yin^{a,*}, John C. Crittenden^{a,b}

^a State Key Laboratory of Water Environment Simulation, School of Environment, Beijing Normal University, Beijing, China

^b School of Civil and Environmental Engineering and The Brook Byers Institute for Sustainable Systems, Georgia Institute of Technology, Atlanta, GA 30332, USA

ARTICLE INFO

Keywords:

Single-atom alloys
Cu vacancy
Electrocatalysis
Nitrate reduction
Synthetic ammonia

ABSTRACT

Electrocatalytic reduction of nitrate (NO₃[−]) to ammonia (NH₃) in wastewater is a promising economic process for NH₃ synthesis. This work designed and prepared Au₁Cu (111) single-atom alloys with surface Cu vacancies (V_{Cu}-Au₁Cu SAAs), which exhibited superior NH₃ Faradaic efficiency (98.7%) with a production rate of 555 μg h^{−1} cm^{−2} at −0.2 V vs. RHE, while negligible activity decay was found after a durability test. Meanwhile, 97% of produced NH₃ can be recovered by a simple membrane distillation. Characterizations evidence that electron migration from Cu to Au atoms creates electron-deficient Cu active sites in V_{Cu}-Au₁Cu SAAs, which promote the generation of active hydrogen species (*H) that can readily hydrogenate NO₃[−]. Theoretical calculation reveals that the bi-functional Cu sites not only promote the activation of water to produce *H but also lower the energy barrier of *NH₃ desorption from the catalyst surface.

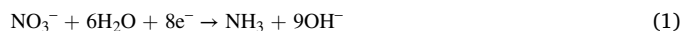
1. Introduction

Electrocatalytic NH₃ synthesis powered by renewable energy as a green and appealing route to generate value-added chemicals has received intense interest. This process offers a potential alternative to the traditional energy intensive Haber-Bosch process, by which nitrogen (N₂) and hydrogen (H₂) are reluctantly converted to NH₃ under extremely high pressure and temperature [1,2]. Recent studies have shown that NH₃ can be synthesized by N₂ and water (H₂O) through electrochemical methods under ambient conditions [3,4]. Unfortunately, the N₂ fixation efficiency is fairly low owing to the poor N₂ solubility in H₂O and the high energy barrier of N≡N bond cleavage (941 kJ mol^{−1}) [5,6], resulting in a pessimistic NH₃ yield rate, which is nearly three orders of magnitude lower than that of industrial synthetic NH₃ [7].

Compared with the highly stable N₂ molecule, NO₃[−] could be a promising nitrogen source for large-scale electrochemical NH₃ synthesis [8]. The high solubility of NO₃[−] in aqueous solution and the low dissociation energy (204 kJ mol^{−1}) of N=O bond facilitates the reaction kinetics of NH₃ generation [9,10]. In addition, NO₃[−] has become one of the most common water contaminants due to the excessive use of nitrogen fertilizers and fuel combustion. Its rich accumulation leads to the deterioration of water quality and threatens human health [11]. Therefore,

the electrocatalytic NO₃[−] reduction to NH₃ reaction (NITRR), as a means of converting wastes into value-added products, provides an excellent way to solve environmental and energy problems [12–17]. In view of the above advantages, synthesizing electrocatalysts that can reduce NO₃[−] to NH₃ with high selectivity and stability has attracted great interest. At present, some novel efficient electrocatalyst, such as CoP nanosheet arrays [18], Pd-doped TiO₂ nanoarray [19], Pd-incorporated Cu₂O [20], single-atom Cu [21], and Co-doped Fe@Fe₂O₃ [22] have been developed to promote the NITRR.

Although the NITRR is attractive, the selectivity and efficiency of NITRR (Eq. (1)) were severely limited by its sophisticated eight-electron reaction process and the undesired side H₂ evolution reaction (HER, Eq. (2)) [7].



Besides, the complicated side reactions of forming N₂, nitrite (NO₂[−]), hydrazine (N₂H₄), and hydroxylamine (NH₂OH), to some extent, interfere with the process of the main NITRR. Therefore, reasonable design and development of electrocatalysts to break scaling relations between intermediates along the reaction path and suppress the HER is the crucial measure to enhance the NITRR activity [23].

* Corresponding author.

E-mail addresses: lfyin@bnu.edu.cn, yinlifeng@gmail.com (L. Yin).

<https://doi.org/10.1016/j.apcatb.2022.121346>

Received 2 January 2022; Received in revised form 28 February 2022; Accepted 22 March 2022

Available online 26 March 2022

0926-3373/© 2022 Elsevier B.V. All rights reserved.

Cu-based catalysts have been frequently reported for their high NITRR efficiency [24]. Among the reported design strategies, alloying Cu with heterogeneous elements is considered a valuable avenue to enhance its performances. This is because alloying could reconstruct the surface atomic structure and optimize the binding strength between reactants and active sites [16]. Previous reports have shown that introducing the noble metal (Au or Ag) to the Cu surface improved the CO₂ electroreduction reaction and suppressed that of HER by tuning the adsorption free energy of hydrogen (ΔG_H) [25]. More recently, single-atom catalysts have aroused a broad concern with the merits of nearly 100% atomic utilization, operable coordination environment and well-defined active sites [26]. Single-atom alloys (SAAs), a low number of isolated metal atoms disperse onto the surface of a metal host, married the advantages of bimetallic alloys and single atoms and showed excellent catalytic properties [27]. In addition, recent studies show that manufacturing surface metal atomic vacancies is another effective strategy for enhancing a metal's catalytic properties [28,29]. These studies inspire us to combine SAAs and metal atomic vacancy to engineer the metal catalyst surface at the atomic scale for the boosting of NITRR.

In this work, two-dimensional Cu nanosheets (Cu NSs) with (111) single crystal surface were synthesized as a host metal owing to its large surface area and high selectivity for NITRR to NH₃ [30,31]. A small amount of Au atomically dispersed on Cu (111) surface to fabricate Au₁Cu SAAs and further constructed Cu vacancies on their surface (V_{Cu}-Au₁Cu SAAs), which shows a desirable NITRR activity and selectivity. We demonstrate that single Au atoms and Cu vacancies work synergistically on the neighboring Cu atoms, resulting in electron transfer from Cu to Au. Furthermore, theoretical insights into the synergistic effect between single-atom alloys and surface defects further assist in fundamentally understanding the exceptional catalytic performance of V_{Cu}-Au₁Cu SAAs.

2. Experimental section

2.1. Catalyst preparation

2.1.1. Synthesis of Cu NSs

Cu NSs were prepared by the previously reported chemical reduction method [30]. Initially, 0.4 g of Cu(NO₃)₂·3 H₂O was dissolved in 120 mL deionized water (DI), and 0.9 g of L-ascorbic acid was added. After stirring for 10 min, 0.9 g of hexadecyltrimethylammonium bromide (CTAB) and 0.9 g of hexamethylenetetramine (HMTA) were added to the above solution and stirred vigorously for 30 min. Next, the prepared precursor solution was sealed and heated to 80 °C and maintained for 3 h. The resulting dispersion was centrifuged, washed several times with DI and ethanol and dried in vacuum at 60 °C for 6 h.

2.1.2. Synthesis of V_{Cu}-Au₁Cu SAAs

Au₁Cu SAAs were first synthesized by a typical galvanic replacement process [32,33]. Fresh Cu NSs (200 mg) were ultrasonically dispersed in 100 mL HCl aqueous solution (2 mmol L⁻¹) under N₂ protection. Subsequently, an aqueous solution of HAuCl₄·3 H₂O (17 mL, 0.30 mmol L⁻¹) was added dropwise to the above dispersion. After that, the mixture was heated to 100 °C for 20 min. The Au₁Cu SAAs were obtained by filtration, washing and vacuum drying. Finally, the Au₁Cu material was dispersed in 10 mL CH₃COOH and heated to 60 °C. After stirring for 1 h, the resulting V_{Cu}-Au₁Cu product was centrifuged, washed with ethanol and dried in vacuum. ICP-OES determined that the Au content is 0.41 wt %. For comparison, V_{Cu}-M₁Cu (M = Pt, Pd, Ru) was prepared with the same method. H₂PtCl₆·6 H₂O, K₂PdCl₄, and RuCl₃ were used as the metal precursors for Pt, Pd, and Ru, respectively.

2.1.3. Synthesis of V-Cu NSs

V-Cu NSs were synthesized by the same acid-etching dealloying method as that outlined for V_{Cu}-Au₁Cu SAAs. The only difference is that

fresh Cu NSs underwent acidic leaching to produce Cu vacancies.

2.2. Materials characterization

The detailed information of characterization techniques is provided in Text S1.

2.3. Electrochemical measurements

All electrochemical measurements were carried out under room temperature in a typical H-type cell, which is separated into two chambers by a Nafion 117 membrane (Fig. S1). Before testing, the Nafion 117 membrane was successively treated in 5% H₂O₂ and 0.5 M H₂SO₄ at 80 °C for 1 h, and finally washed several times with DI. An AMETEK VersaSTAT 3 electrochemical station was used to control the electrolysis reaction. Ag/AgCl reference electrode (saturated KCl) and the working electrode were placed in the cathode chamber, while platinum plates (2 cm × 2 cm) counter electrode was placed in the anode chamber. The samples were coated on AvCarb P75 carbon paper (2.0 cm × 1.5 cm, thickness of 0.245 mm) to prepare the working electrode: 6 mg samples, 960 μL ethanol, and 40 μL Nafion solution (Sigma Aldrich, 5 wt%) were mixed and ultra-sonicated for 1 h to get a homogeneous catalyst ink. Then, a proper volume of ink was drop-cast onto carbon paper with a loading of 0.8 mg cm⁻². 0.1 M KOH electrolyte (90 mL, pH = 13.1) was equally distributed to the anode and cathode chambers. This alkaline electrolyte can not only inhibit the side HER, but also facilitate the migration and activation of NO₃⁻ [15]. On the hand, the potentials in this study were converted to the reversible hydrogen electrode (RHE) potential: $E_{RHE} = E_{Ag/Cl} + 0.197 \text{ V} + 0.059 \text{ pH}$. Therefore, the slight fluctuation of pH of the alkaline electrolyte during the reaction has little effect on the working potential.

The size of the working electrode immersed in electrolyte is 1.5 × 1.5 cm². For the electrocatalytic NITRR, KNO₃ was added to the cathode electrolyte (containing 7.14 mM NO₃⁻). During the reaction, a high purity argon flow (10 mL min⁻¹) was continuously injected into the cathode cell, and the electrolyte was stirred at a rate of 200 rpm. NITRR experiments were carried out at different potentials for 3 h to evaluate the performance of the catalyst. The linear sweep voltammetry (LSV) was conducted at a rate of 5 mV s⁻¹. The electrochemical impedance spectroscopy (EIS) was performed at -0.2 V vs. RHE from 0.01 to 10⁵ Hz, and the AC amplitude was set to 10 mV. For the stability test, the NITRR was carried out at -0.2 V vs. RHE at a stirring rate of 200 rpm. The electrolyte solution was changed every 3 h, and the above experiment was repeated 5 times with the same working electrode. All current densities reported in this work are based on geometric surface area.

2.4. Products detection and analysis

Suppressed conductivity ionic chromatography (Dionex ICS-6000) was used to detect variations in NO₃⁻ and NO₂⁻ concentrations with electrolysis time. Due to the large ion concentration, the reaction solution was diluted 10 times to achieve a better signal separation effect. The concentration of NH₄⁺ was quantified with an ultraviolet-visible (UV-Vis) spectrophotometer (HACH DR6000) by using Nessler's reagent as the developer at 420 nm. The calibration curves of NO₃⁻, NO₂⁻ and NH₄⁺ were established using standard KNO₃, KNO₂, and NH₄Cl solutions. The resulting NH₃ concentration was also determined by ¹H nuclear magnetic resonance (¹H NMR) spectroscopy. The ¹H NMR signal was recorded on a Bruker Avance II 500 MHz system through water suppression. For the isotopic labeling experiments, 7.14 mM K¹⁵NO₃/0.1 M KOH mixed solution was used as the cathode electrolyte. After 3 h of the ¹⁵NO₃⁻ reduction reaction at -0.2 V vs. RHE, the ¹⁵NH₄⁺ in the reaction solution was detected by ¹H NMR (500 MHz) spectroscopy. Furthermore, N₂H₄ as a possible product was detected by Watt and Chrisp's method [34].

The Faradaic efficiency (FE) for NO₃⁻ electroreduction to NH₃ can be

calculated according to the following formula:

$$FE = (8 \times F \times C \times V) / (M \times Q)$$

where F is the Faradaic constant ($96,485 \text{ C mol}^{-1}$), C is the measured mass concentration of NH_3 , V is the volume of the cathode electrolyte, M is the relative molar mass of NH_3 , and Q is the total charge flowing through the working electrode.

The selectivity of synthesizing NH_3 can be calculated using as follows:

$$\text{Selectivity} = (C_{\text{NH}_3} / \Delta C_{\text{NO}_3^-}) \times 100\%$$

where C_{NH_3} represents the mass concentration of NH_3 and $\Delta C_{\text{NO}_3^-}$ is the mass concentration difference of NO_3^- electrolysis before and after 3 h.

The electrical energy per order (E_{EO}) is calculated to benchmark the required electric energy to reduce the NO_3^- concentration by 1 order of magnitude in a unit volume (kWh m^{-3}) according to the following formula [14]:

$$E_{\text{EO}} = (E_{\text{cell}} \times I \times t) / (V_s \times \log(C_0/C_t))$$

where E_{cell} is the applied cell's potential (V), I is the current (A), t is the time (h), V_s is the volume of the cathode electrolyte (L), C_0 and C_t are the initial and final concentrations of NO_3^- (mol L^{-1}).

2.5. Computational method

Density functional theory (DFT) calculations were performed using the Vienna ab Initio simulation program (VASP 5.4.4) [35,36]. The electron-ion interactions were described by the projector augmented wave (PAW) method [37]. The exchange-correlation was described by generalized gradient approximation (GGA) with the Perdew-Burke-Ernzerhof (PBE). An energy cut-off of 400 eV was used. The convergence criterion for the residual force and energy on atoms converged to less than $0.02 \text{ eV } \text{\AA}^{-1}$ and 10^{-5} eV , respectively. Reciprocal space was described by using the Monkhorst-Pack scheme to generate a $3 \times 3 \times 1$ k points [38]. The transition state (TS) of water dissociation was carried out by nudged elastic band (NEB) method. Detailed calculation information about water dissociation and nitrate reduction reactions on the catalyst surface can be obtained in Text S2.

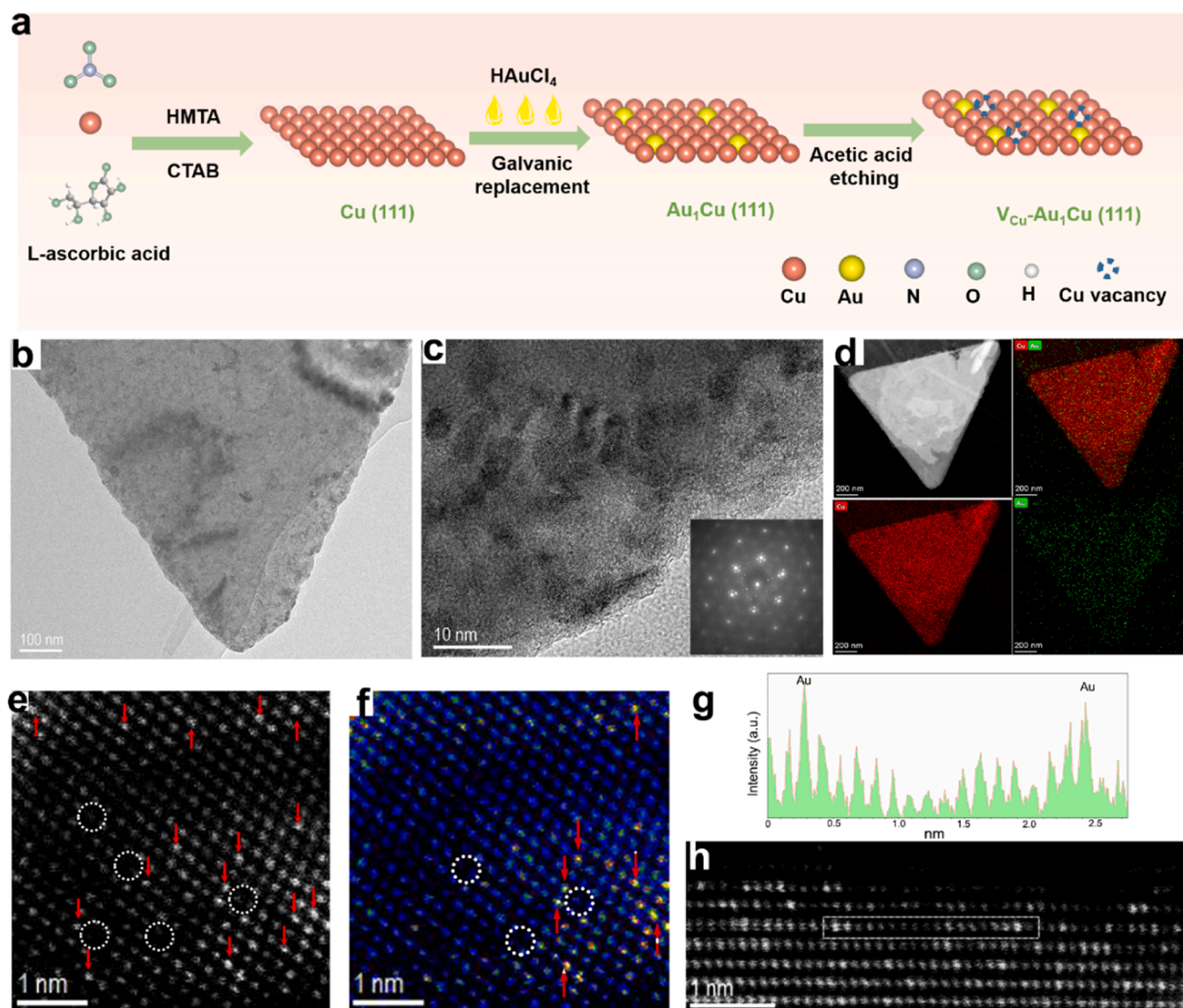


Fig. 1. (a) Schematic diagram of the $\text{V}_{\text{Cu}}\text{-Au}_1\text{Cu}$ SAAs synthetic procedure. (b) TEM and (c) HRTEM images of $\text{V}_{\text{Cu}}\text{-Au}_1\text{Cu}$ SAAs (inset in c shows the corresponding FFT pattern of $\text{V}_{\text{Cu}}\text{-Au}_1\text{Cu}$ SAAs). (d) EDS mapping of $\text{V}_{\text{Cu}}\text{-Au}_1\text{Cu}$ SAAs to show the distribution of Cu and Au elements. (e) HADDF-STEM image and (f) the corresponding colored intensity map of $\text{V}_{\text{Cu}}\text{-Au}_1\text{Cu}$ SAAs. Red arrows highlight Au atoms, and the white circle areas indicate the vacancy of Cu atoms. (g) The corresponding intensity profile from the region marked by the white dashed rectangle in image (h) (a typical region of the $\text{V}_{\text{Cu}}\text{-Au}_1\text{Cu}$ SAAs).

3. Results and discussion

3.1. Preparation and structural characteristics of V_{Cu} -Au₁Cu SAAs

The V_{Cu} -Au₁Cu SAAs were synthesized by a three-step process (Fig. 1a). First, single crystal Cu (111) NSs were prepared by a simple chemical reduction route. Then, the Au₁Cu SAAs were synthesized via galvanic replacement (GR) method by replacing Cu on Cu NSs with Au [27]. As the standard redox potential of Au^{3+}/Au (0.93 V) is much higher than that of Cu^{2+}/Cu (0.34 V), it is favorable for Au^{3+} to be reduced by the Cu support, which is confirmed by UV-vis spectroscopy analysis (Fig. S2). After that, the Au₁Cu SAAs were dispersed in acetic acid. After acid-etching dealloying for 1 h, the solution turned blue (Fig. S3), indicating that part of the Cu^{2+} on the Au₁Cu SAAs was leached, resulting in Cu vacancies (V_{Cu} -Au₁Cu SAAs). The transmission electron microscopy (TEM) image indicates that the prepared Cu NSs were triangular with a smooth surface on a micrometer-scale (Fig. S4a). The high-resolution TEM (HRTEM) image and the fast Fourier transform (FFT) pattern (Fig. S4b, c) indicate that the lattice is distorted with large

period striations, which is caused by the Moiré effect arising from the overlapping nanosheets [39]. Next, the atomic-resolution TEM was carried out to directly observe the arrangement of Cu atoms (Fig. S4d, e). Clear lattice fringes with interplanar spacing of 0.208 nm were observed, corresponding to the Cu (111) crystal plane.

Compared with Cu NSs, the TEM image of the V_{Cu} -Au₁Cu SAAs also displays a triangular nanosheet morphology. However, the borders of the product were slightly serrated (Fig. 1b). Furthermore, some dark pits with a size of approximately 2–4 nm on the sample surface were observed in Fig. 1c, which was attributed to the Cu vacancies caused by the leaching of surface Cu atoms [29,40]. The FFT pattern inset in Fig. 1c shows that the V_{Cu} -Au₁Cu SAAs maintained the face-centered cubic structure along the (111) alloy plane. The energy dispersive spectroscopy (EDS) mapping results indicate that Au and Cu were uniformly distributed over the entire architecture (Fig. 1d). Aberration-corrected high-angle annular dark-field scanning TEM (HAADF-STEM) was used to analyze the architecture of the V_{Cu} -Au₁Cu SAAs (Fig. 1e), which displays several bright atom-sized points (marked by red arrows) dispersed on the crystal surface, indicating that the atomically dispersed

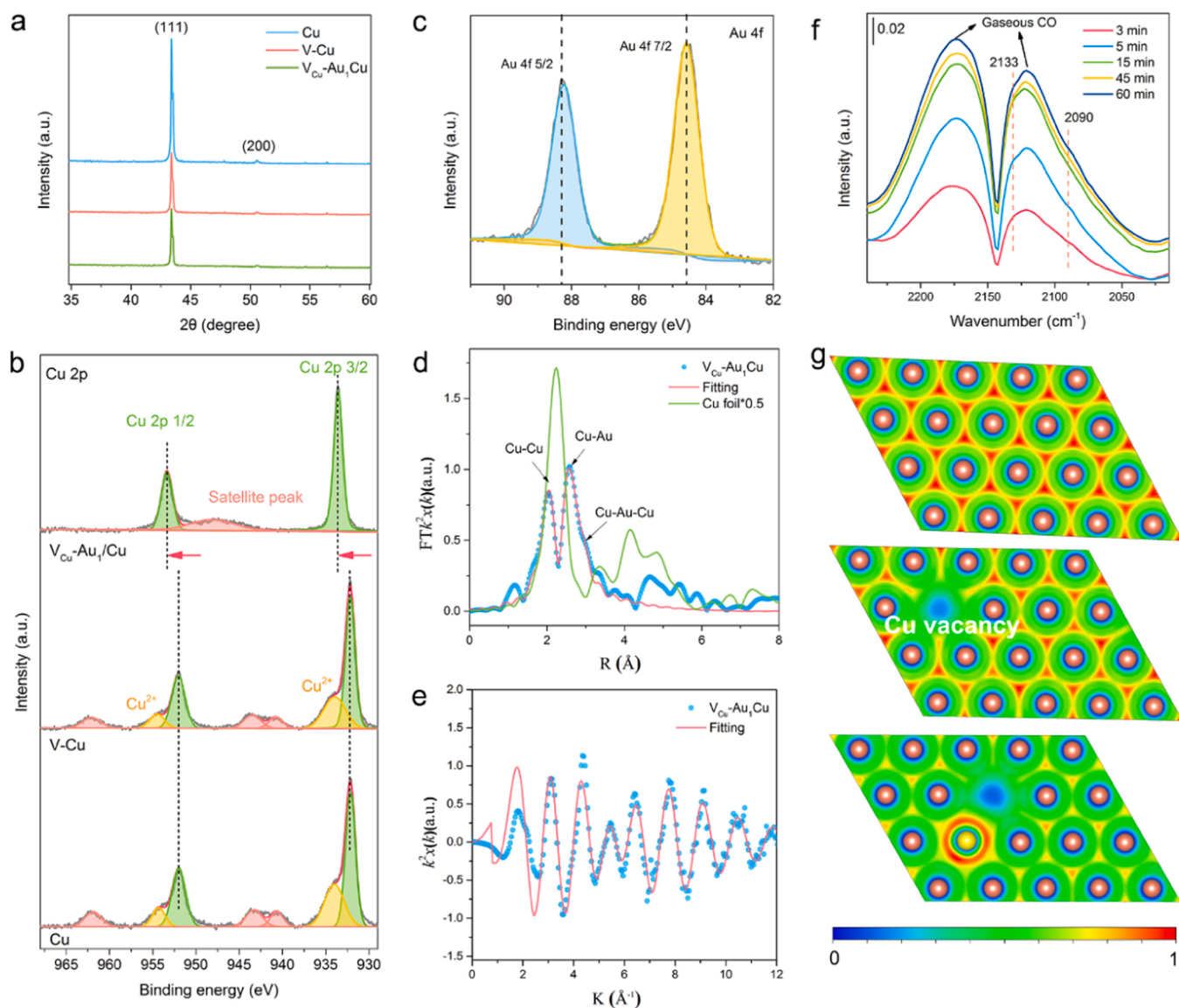


Fig. 2. (a) XRD patterns and (b) High-resolution XPS spectra of Cu 2p for the Cu NSs, V-Cu NSs and V_{Cu} -Au₁Cu SAAs. (c) High-resolution XPS spectra of Au 4f for the V_{Cu} -Au₁Cu SAAs. (d) The EXAFS spectra of the Cu foil and V_{Cu} -Au₁Cu SAAs. (e) Corresponding Cu K-edge EXAFS fitting curve of V_{Cu} -Au₁Cu SAAs in k space. (f) In situ DRIFT spectra of V_{Cu} -Au₁Cu SAAs under CO flow at different times. (g) Differential charge densities of the Cu NSs (top), V-Cu NSs (middle), and V_{Cu} -Au₁Cu SAAs (bottom). Blue: charge depletion, red: charge accumulation.

Au sites are isolated by surrounding Cu atoms. Additionally, many lattice defects without atomic arrangement (marked by white circles) were clearly observed, further proving that Cu vacancies were produced. The corresponding colored intensity map in Fig. 1f enables us to better identify the distribution of single Au atoms and Cu vacancies. It can be observed that different atoms have obvious contrast in electron intensity, in which high-energy atoms (Au single atoms) correspond to bright golden dots (marked by red arrows), and low-energy atoms (Cu atoms) show blue color, while, Cu vacancies on the crystal surface show black (marked by white circles) due to the weakest electron intensity. To further strengthen this result, the HADDF intensity profile was measured from the white dashed rectangle region shown in Fig. 1h. The intensity data (Fig. 1g) shows that isolated Au atoms and Cu vacancies coexist on the surface. TEM images also reveal Cu vacancies in the synthesized V-Cu NSs sample (Fig. S5).

X-ray diffraction (XRD) was used to determine the crystal structure of the as-prepared catalysts (Fig. 2a). All the samples show a main diffraction peak at 43.4° and a minimal peak at 50.5° , which can be ascribed to the (111) and (200) facets of the Cu base [41], respectively, further confirming that the as-prepared samples are face-centered cubic structure. The XRD patterns reveal that the crystal phase is unchanged, demonstrating that the changes caused by alloying and acid-etching are limited to the sample surface [10]. To investigate the surface atom chemical states, X-ray photon spectroscopy (XPS) spectra were obtained. The Cu 2p XPS spectra exhibited in Fig. 2b were first analyzed. The main peaks in Cu NSs at approximately 932.1 eV and 952.0 eV were assigned to the 2p $3/2$ and 2p $1/2$ of Cu⁰, respectively. The binding energies at 934.0 eV and 954.3 eV are assigned to Cu²⁺, and the peaks at 940.7 eV, 943.3 eV, and 961.9 eV correspond to the satellite peaks of Cu²⁺, indicating that the high-density surface Cu atoms were partially oxidized [42]. The XPS results of V-Cu NSs exhibited a very similar Cu 2p binding energy with respect to Cu NSs. Notably, the binding energies of Cu⁰ for V_{Cu}-Au₁Cu SAAs have a 0.21 eV positive shift compared with Cu or V-Cu NSs, indicating that the electrons are transferred from Cu to Au atoms, during which Cu atoms around Au act as electron donors and become electron deficient [43]. In addition, no Cu²⁺ peaks were found in the V_{Cu}-Au₁Cu SAAs, which implies that the strong electronic effect among Cu and Au atoms inhibits the oxidation of Cu atoms on the catalyst surface after alloying. The remarkable change in electronic properties induced by the alloying effect may contribute to the NITRR [44]. In the Au 4f spectrum of V_{Cu}-Au₁Cu SAAs, two characteristic peaks at 84.6 eV and 88.3 eV were assigned to Au 4f $7/2$ and Au 4f $5/2$ (Fig. 2c), which can be attributed to ionic Au⁺, meaning that no Au nanoparticles were formed on the sample [45,46]. The XPS data show that the surface Au concentration (0.36 atom %) was much higher than the overall Au loading (0.13 atom %), indicating that most of the introduced Au species exist in the surface or subsurface layer Cu support. To delving into the electronic structure of the as-prepared catalysts, X-ray absorption spectroscopy (XAS) was conducted. As shown in the extended X-ray absorption fine structure (EXAFS) collected at Cu K-edge (Fig. 2d), the V_{Cu}-Au₁Cu SAAs exhibit a coordination shell at 2.1 Å corresponding to the Cu-Cu first shell and two other shells at 2.5 Å and 2.9 Å, which were associated with the Cu-Au and Cu-Au-Cu contributions [47], respectively, supporting Au-Cu alloy formation. Based on the fitting results (Figs. 2e, S6, Table S1), the coordination numbers (CN) of Cu-Au and Cu-Au-Cu were estimated to be 9.2 and 7.9, respectively, which are close to the CN of previously reported Cu based SAAs [47,48]. From the Au L₃-edge investigation of V_{Cu}-Au₁Cu SAAs (Fig. S7, Table S2), it can be found that the Au had a CN of 4.1 ± 0.3 (much smaller than 12) in the first shell. The lower CN of Au indicates that most of the Au atoms are coordinately unsaturated and located on the surface [49]. In addition, no Au-Au coordination shell was found, indicating that Au atoms in the catalysts were isolated by surrounding Cu atoms [48].

To further verify the change in surface structure caused by the alloying process, in situ diffuse reflectance infrared Fourier transform (DRIFT) spectroscopy experiments were performed [50], which can

commendably reflect the dispersion and oxidation state of active sites through CO molecule probe. The DRIFT spectra of the Cu NSs and V-Cu NSs in a 5 vol% CO/Ar premixed gas flow is shown in Fig. S8. Two broad adsorption bands centered at 2118 cm^{-1} and 2173 cm^{-1} were attributed to the P and R branches of gaseous CO, respectively [49,51]. The shape of the peak centered at 2118 cm^{-1} is asymmetric, which arises from its overlap with CO adsorbed on the Cu surface ($2090\text{--}2197\text{ cm}^{-1}$) [52]. As shown in Fig. 2d, CO adsorption on the V_{Cu}-Au₁Cu SAAs produces a small feature at 2133 cm^{-1} corresponding to Au⁺-CO species, demonstrating the atomically dispersed Au in V_{Cu}-Au₁Cu SAAs. Moreover, it also showed that the valence of the Au atom is +1, which is in full agreement with the XPS result.

Based on the above experimental results, we constructed ideal Cu (111), V-Cu (111), and V_{Cu}-Au₁Cu (111) models with five atomic layers (Fig. S9), and first-principles calculations were carried out to investigate the effect of Cu vacancies and Au atoms on the electronic structure at the atomic level. The charge density difference of the samples is visualized in Fig. 2g. It can be seen that the neighboring Cu atoms of V_{Cu} in the V-Cu NSs obtain fewer charges than those on the Cu NSs. The charge density has a significant redistribution when the Au atom replaces one of the neighboring Cu atoms in V_{Cu} (Fig. 2g, bottom). The charges are more accumulated or localized in the vicinity of Au, resulting in charge depletion not only in the neighboring Cu atoms of V_{Cu} and Au sites but also in the normal Cu atoms, indicating that there is an obvious charge transfer between the Au and Cu atoms in V_{Cu}-Au₁Cu SAAs. The charge density reconfiguration caused by the strong interaction between Cu, Au, and V_{Cu} is potentially responsible for the catalytic activity and selectivity [53].

3.2. Electrocatalytic NITRR performance

The NITRR performance of different samples were performed in a H-type cell under argon atmosphere and ambient conditions. As revealed by LSV performed in KNO₃/KOH electrolyte (Fig. 3a), the onset potential of V_{Cu}-Au₁Cu SAAs for NO₃⁻ reduction is 0.3 V vs. RHE, which was much more positive than that of Cu NSs or V-Cu NSs (0.1 V vs. RHE). Here, the potential at a current density of 1 mA cm^{-2} is defined as the onset potential. In addition, the V_{Cu}-Au₁Cu SAAs exhibit the highest current densities among the three samples. These results suggested that the NO₃⁻ electroreduction reaction occurs more readily on the V_{Cu}-Au₁Cu SAAs. Although Cu NSs and V-Cu NSs show the same NO₃⁻ reduction onset potential, the current density of V-Cu NSs is significantly higher than that of Cu NSs when the potential is lower than 0 V vs. RHE, indicating that Cu vacancies can also improve the catalytic activity. As presented in Fig. 3b, the resulting Tafel slopes are 94, 43, and 28 mV dec^{-1} for Cu NSs, V-Cu NSs, and V_{Cu}-Au₁Cu SAAs, respectively. Thus, V_{Cu}-Au₁Cu SAAs have the highest NITRR reaction kinetics and intrinsic activity due to the lowest Tafel slope value. It is considered that the electrochemical active surface area (ECSA) is the most discriminative evaluation method for reflecting electrochemical intrinsic activity [54]. The ECSA values were estimated in this work by the electrochemical double-layer capacitance (C_{dl}) measurement method [55]. C_{dl} can be inferred by performing cyclic voltammetry (CV) at different scan rates in a non-Faradaic current region (Fig. S10). As displayed in Fig. 3c, the C_{dl} of V_{Cu}-Au₁Cu SAAs is 4.3 mF cm^{-2} , much larger than the values of Cu NSs (1.4 mF cm^{-2}) and V-Cu NSs (mF cm^{-2}), suggesting that V_{Cu}-Au₁Cu SAAs have the largest ECSA, which could be due to the electronic structure of the catalyst being tuned by Cu vacancies and Au atoms and thus leading to an increase in active reaction sites. Furthermore, the charge-transfer resistances during the electrochemical process were measured by EIS. The V_{Cu}-Au₁Cu SAAs show a smaller Nyquist semi-circle diameter (Fig. 3d), correlating to the fast charge-transfer kinetics in the NO₃⁻ reduction reaction.

Next, NITRR was performed to evaluate the positive effects brought by the vacancies and alloying. The possible products of NO₂⁻, NH₃ and N₂H₄ were quantified by ion chromatography (IC), UV-Vis

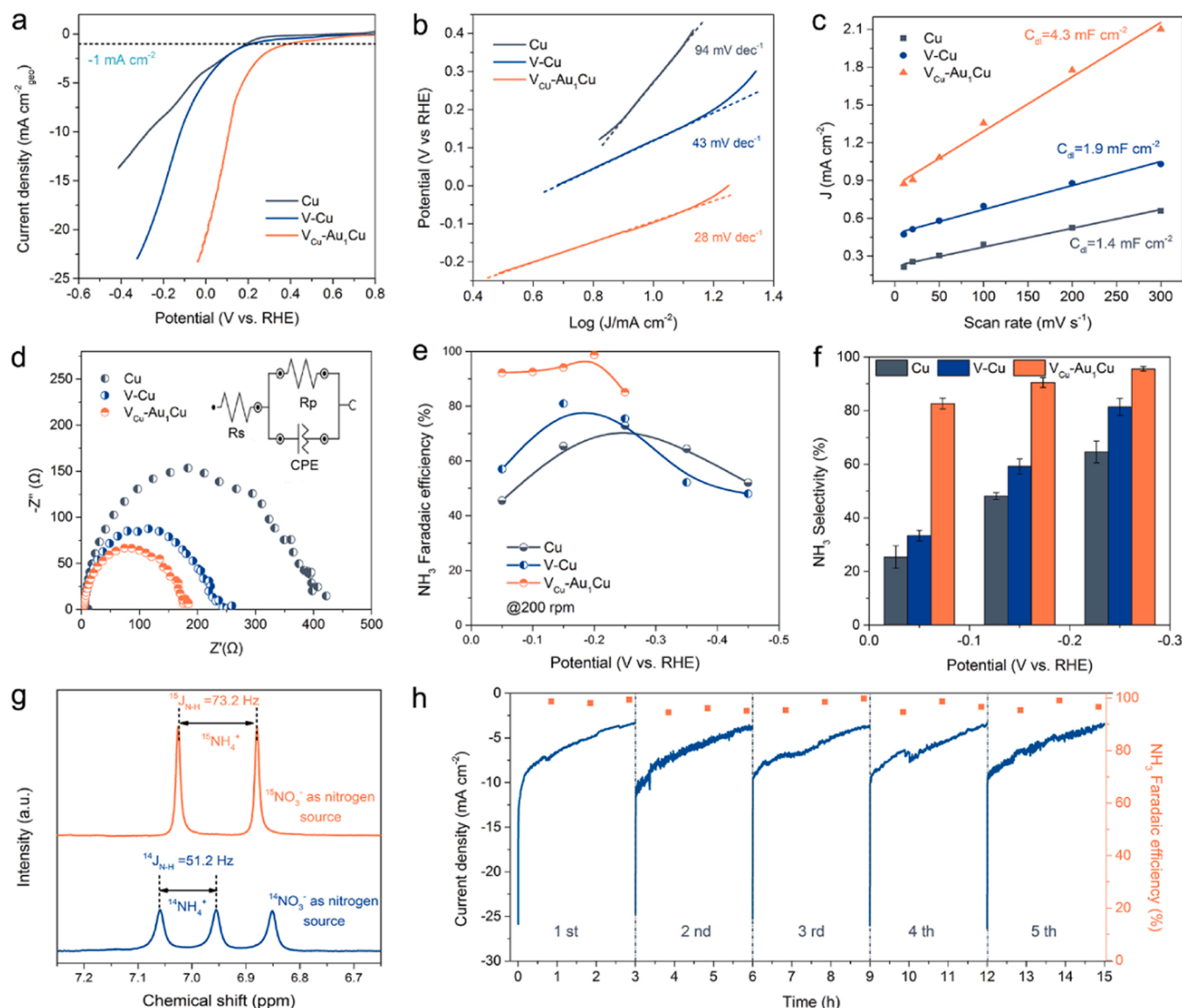


Fig. 3. Electrocatalytic NITRR performance of Cu NSs, V-Cu NSs and $V_{Cu}-Au_1Cu$ SAAs. (a) LSV curves tested in KNO_3/KOH electrolyte. (b) Corresponding Tafel plots of the samples. (c) Capacitive current as a function of the scan rate of the samples. (d) Nyquist plots of the samples at -0.2 V vs. RHE in KNO_3/KOH electrolyte. (e) NH_3 FE and (f) selectivity of various samples at each given potential. (g) 1H NMR spectra of NITRR at -0.2 V vs. RHE by $V_{Cu}-Au_1Cu$ SAAs using $^{14}NO_3^-$ and $^{15}NO_3^-$ as the nitrogen source. (h) Stability test (repeated five cycles) and corresponding NH_3 FE (orange squares) of $V_{Cu}-Au_1Cu$ SAAs. The initial NO_3^- concentration in each cycle is 7.14 mM.

spectrophotometry and 1H NMR, respectively (Figs. S11–S13). According to the results (Figs. S14–S16), NH_3 and NO_2^- were the major products at all potentials as time changed, and no N_2H_4 was detected. All samples showed the same trend; that is, with increasing cathode potential, the yield and selectivity of NH_3 increased, while the yield and selectivity of NO_2^- decreased. Notably, $V_{Cu}-Au_1Cu$ SAAs exhibited a much higher NH_3 yield and selectivity than Cu NSs and V-Cu NSs at any given cathode potential, further highlighting the synergistic role of the alloy and vacancy. Fig. 3e displays the potential-dependent NH_3 FEs obtained with Cu NSs, V-Cu NSs, and $V_{Cu}-Au_1Cu$ SAAs. In all of the experiments, $V_{Cu}-Au_1Cu$ SAAs were superior to the other samples and reached ca. 98.7% NH_3 FE at -0.2 V vs. RHE, corresponding to a yield rate of approximately $555 \mu g h^{-1} cm^{-2}$ (Fig. S17). In contrast, Cu NSs have a relatively low NH_3 FE of 72.9% at -0.25 V vs. RHE, delivering a yield rate of $322 \mu g h^{-1} cm^{-2}$, while the V-Cu NSs show an optimal FE of 81.1% at -0.15 V vs. RHE with an NH_3 yield rate of $332 \mu g h^{-1} cm^{-2}$. The NH_3 FE showed a decreasing trend after -0.2 or -0.25 V vs. RHE, mainly due to the competitive HER gradually gaining ground at high

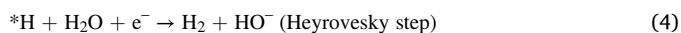
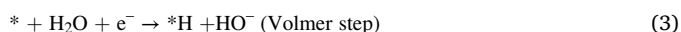
potentials [56]. It is noteworthy that pure carbon paper electrode cannot produce NH_3 at -0.25 V vs. RHE. Even at a more negative potential of -0.45 V vs. RHE, the NH_3 yield rate is only $15.5 \mu g h^{-1} cm^{-2}$ (Fig. S18). This suggests that carbon paper has little contribution to NH_3 yield when the potential is higher than -0.45 V vs. RHE. In contrast, $V_{Cu}-Au_1Cu$ SAAs still keep a high NH_3 FE of 66.5% at 0.0 V vs. RHE, and can start the NITRR at 0.2 V vs. RHE with NH_3 FE of 14.3% (Fig. S19). As shown in Fig. 3f, $V_{Cu}-Au_1Cu$ SAAs displayed the best NH_3 selectivity, as high as 94.5% at -0.25 V vs. RHE, much higher than that of Cu NSs (64.6%) and V-Cu NSs (81.4%) at the same potential. Notably, the NITRR capability over the $V_{Cu}-Au_1Cu$ SAAs in terms of NH_3 FE and selectivity is satisfied compared with the most of recent reported catalysts (Table S3). Moreover, to explore the superiority of Au single atoms promoting the NITRR, the control experiment in Au nanoparticles supported on Cu NSs with surface Cu vacancies ($V_{Cu}-Au_{NP}Cu$) is performed (Fig. S20). The content of Au in the $V_{Cu}-Au_{NP}Cu$ is 3.6 wt% determined by ICP-OES. Distinctly, the NH_3 FE and selectivity of $V_{Cu}-Au_{NP}Cu$ are much lower than that of $V_{Cu}-Au_1Cu$ at the same potential. We further prepared the Au_1Cu SAAs

on Cu powder ($V_{\text{Cu-Au}_1\text{Cu}}$ powder) and Cu nanocubes ($V_{\text{Cu-Au}_1\text{Cu}}$ nanocubes) to prove that Au single atoms play an important role in improving the activity of Cu based catalysts (Fig. S21). It is evident that $V_{\text{Cu-Au}_1\text{Cu}}$ powder and $V_{\text{Cu-Au}_1\text{Cu}}$ nanocubes have better intrinsic activity than those of defective Cu powder and Cu nanocubes.

To verify the source of synthesized NH_3 , an isotopic labeling study was conducted by ^1H NMR (Fig. 3g). Three peaks with spacing of 51.2 Hz were observed after 3 h of electrolysis in $\text{K}^{14}\text{NO}_3/\text{KOH}$ electrolyte under -0.2 V vs. RHE, corresponding to the standard $^{14}\text{NH}_4^+$ solution [57]. The synthesized NH_3 was quantified by the $^{14}\text{NH}_4^+$ calibration curve (Fig. S12c), achieving an NH_3 FE of 94.8%, which was consistent with the quantitative results of the spectrophotometric method. Only double peaks with a spacing of 73.2 Hz corresponding to $^{15}\text{NH}_4^+$ were obtained in ^1H NMR spectra when using $\text{KOH}/\text{K}^{15}\text{NO}_3$ as the electrolyte, suggesting that the produced NH_3 originated from electrochemical NITRR. Meanwhile, no NH_3 was detected in the KOH electrolyte without KNO_3 (Fig. S22), further confirming that the NH_3 produced is not from foreign impurities. In addition, the durability of $V_{\text{Cu-Au}_1\text{Cu}}$ SAAs was measured by five consecutive cycling tests at -0.2 V vs. RHE (Fig. 3h). With the progress of the reaction, the NO_3^- concentration in the cathode chamber gradually decreased, resulting in the gradual decrease of the current density. The reaction solution is renewed every 3 h of the test cycle, so the current density is restored at the beginning of the next cycle. The NH_3 FE was steady and remained at 98%, indicating the favorable stability of $V_{\text{Cu-Au}_1\text{Cu}}$ SAAs for NO_3^- electroreduction. The catalyst after the reaction has also been analyzed by XRD and HADDF-STEM, which showed that the crystal and morphology structure of the $V_{\text{Cu-Au}_1\text{Cu}}$ SAAs remained unchanged after the cyclic reaction (Figs. S23 and S24). Moreover, XPS results showed that the oxidation state of Au species did not change before and after the reaction (Fig. S25), suggesting Au^+ has good stability on the Cu surface due to their strong electron interaction, which is consistent with reported previously [46]. In addition, the E_{EO} was calculated to determine the operational costs of energy-dependent during NITRR. As shown in Fig. S26, the optimum E_{EO} value for $V_{\text{Cu-Au}_1\text{Cu}}$ SAAs was 8.22 kWh m^{-3} , obviously lower than that of Cu NS (11.54 kWh m^{-3}) and V-Cu NSs (10.81 kWh m^{-3}). Notably, the energy cost of $V_{\text{Cu-Au}_1\text{Cu}}$ SAAs was much lower than the recently reported Cu-Pt electrode for NITRR [14].

3.3. Mechanistic investigation of NITRR

Based on the above results, we conclude that the surface electronic structure of the $V_{\text{Cu-Au}_1\text{Cu}}$ SAAs is jointly modulated by alloy and defect engineering, which makes it exhibit enhanced reaction kinetics and NH_3 selectivity for NITRR [58]. However, the underlying reason for the impact of electronic effects on electrocatalytic properties remains unclear in this work. As shown in Eq. (1), the reduction of NO_3^- to NH_3 also consumes H_2O , so the ability of H_2O dissociation to supply hydrogen source is also crucial to the NITRR [59]. It is worth noting that the high overpotential usually leads to the applied potential for NITRR more negative than that of H_2O splitting, causing competing HER to occur and lowering the NH_3 FE and selectivity [14]. It should be noted that the HER in alkaline media largely depends on the dissociation of H_2O molecules to provide sufficient hydrogen source. Generally, HER pathways occur in alkaline media follow the Volmer and Heyrovsky steps [60]:



In this study, the $V_{\text{Cu-Au}_1\text{Cu}}$ SAAs exhibited excellent NH_3 FE and selectivity. It can be explained that the Au atoms and Cu vacancies can prevent the HER by inhibiting hydrogen-hydrogen coupling (Heyrovsky step). Thus enhancing H_2O activation to generate active hydrogen ($*\text{H}$), and promoting the hydrogenation of reaction intermediates to NH_3 . To verify this inference, electron paramagnetic resonance (EPR)

experiments were performed to capture the produced $*\text{H}$ using 5,5-dimethyl-1-pyrroline-N-oxide (DMPO) in KOH electrolyte at -0.2 V vs. RHE under argon atmosphere [15]. A group of nine signal peaks with an intensity ratio of 1:1:2:1:2:1:2:1:1 can be observed in all samples after electrolysis in KOH aqueous solution for 5 min (Fig. 4a). The coupling constants of all sets of signals are calculated as $a_{\text{N}} = 16.4$ G and $a_{\text{H}} = 22.4$ G, which is consistent with the spin values of the DMPO-H adduct [61], confirming that $*\text{H}$ can be produced by H_2O activation. Notably, the intensity of the DMPO-H signals produced by $V_{\text{Cu-Au}_1\text{Cu}}$ SAAs is the strongest, followed by V-Cu NSs and Cu NSs. As a result, the HER on the surface of $V_{\text{Cu-Au}_1\text{Cu}}$ SAAs is indeed suppressed, enhancing the NH_3 FE and selectivity [62]. To verify whether the $*\text{H}$ generated by H_2O activation was involved in NITRR, EPR spectra were recorded in KOH electrolyte containing different concentrations of KNO_3 (0–100 mM) after electrolysis by $V_{\text{Cu-Au}_1\text{Cu}}$ SAAs (Fig. 4b). It is noted that the signal intensities of DMPO-H decreased with increasing NO_3^- concentration, indicating that $*\text{H}$ can react with the NITRR intermediates to promote its hydrogenation to NH_3 [15].

To understand the $*\text{H}$ formation mechanism, DFT calculations were employed to analyze H_2O dissociation kinetics. The optimized configurations of intermediates involved in H_2O dissociation on Cu NSs, V-Cu NSs, and $V_{\text{Cu-Au}_1\text{Cu}}$ SAAs (111) surfaces are presented in Figs. S27–S29, and the corresponding Gibbs free energy diagrams were displayed in Fig. 4c, which depends on the bonding strength of $*\text{H}_2\text{O}$, $*\text{H}$ and $*\text{OH}$ with the catalyst surface. We found that $\Delta G^*_{\text{H}_2\text{O}}$ values of Cu NSs, V-Cu NSs, and $V_{\text{Cu-Au}_1\text{Cu}}$ SAAs are 0.21, 0.13, and 0.11 eV, respectively, indicating that $V_{\text{Cu-Au}_1\text{Cu}}$ SAAs were more favorable for H_2O adsorption and could capture H_2O molecules more effectively. Moreover, it is worth noting that the water dissociation of Volmer step is particularly critical to the overall reaction rate [63]. Therefore, the kinetics of water dissociation or transition states (TS) should be considered, as shown in Fig. 4c. The $V_{\text{Cu-Au}_1\text{Cu}}$ SAAs experiences an energy barrier of 0.48 eV for water dissociation, being significantly lower than that of Cu NSs (0.85 eV) and V-Cu NSs (0.63 eV), indicating that the introduced Au single-atoms could accelerate water dissociation to $*\text{H}$ from the kinetic viewpoint. In addition, the ΔG^*_{H} value is another vital criterion for $*\text{H}$ formation. The results showed that V-Cu NSs and $V_{\text{Cu-Au}_1\text{Cu}}$ SAAs have a strong $*\text{H}$ binding ability (-0.18 eV and -0.21 eV) compared with Cu NSs (-0.05 eV), thus inhibiting the recombination of $*\text{H}$ to H_2 from the thermodynamic point of view. The above theoretical results can well explain the EPR data. The weak binding of H_2O molecules on the Cu NSs leads to an increased kinetic barrier of H_2O dissociation to $*\text{H}$, while $*\text{H}$ also binds weakly on the Cu NSs, which is favorable for dimerizing $*\text{H}$ to form H_2 , leading to a decrease in the $*\text{H}$ intermediate. This is consistent with the EPR results that Cu NSs have the weakest signal intensity. Instead, $V_{\text{Cu-Au}_1\text{Cu}}$ SAAs (111) shows much lower kinetic energy barrier of H_2O dissociation while hindering $*\text{H}$ dimerization to H_2 [64], which explains the strong DMPO-H signal of $V_{\text{Cu-Au}_1\text{Cu}}$ SAAs in the EPR spectra. It is well known that the HER performances of bimetallic or multimetallic alloys based on Pt, Pd and Ru are promising [65–67]. Therefore, $V_{\text{Cu-M}_1\text{Cu}}$ SAAs ($\text{M} = \text{Pt, Pd, Ru}$) were designed to explore its NITRR performance (Fig. S30). The results show that all the catalysts are significantly inferior to $V_{\text{Cu-Au}_1\text{Cu}}$ SAAs or V-Cu NSs in selective NH_3 synthesis (Fig. S31), further confirming that HER inhibition is critical to obtain high selectivity of NO_3^- conversion to NH_3 . These findings suggest that the local electronic structure of $V_{\text{Cu-Au}_1\text{Cu}}$ SAAs was synergistically regulated by single Au sites and Cu vacancies, thus stimulating the formation of $*\text{H}$ that can be readily utilized by NO_3^- and its intermediates (Fig. 4d).

In addition to controlling HER occurrence, the binding strength of all intermediates involved in NITRR is also crucial for the reactivity and selectivity [53]. Therefore, the NITRR through the deoxidation ($*\text{NO}_3 \rightarrow * \text{NO}_2 \rightarrow * \text{NO} \rightarrow * \text{N}$) and hydrogenation ($* \text{N} \rightarrow * \text{NH} \rightarrow * \text{NH}_2 \rightarrow * \text{NH}_3$) elementary steps were calculated to understand the relationship between the binding degree of intermediates and NITRR activity [15]. The optimized structures of all intermediates on Cu NSs (111), V-Cu NSs

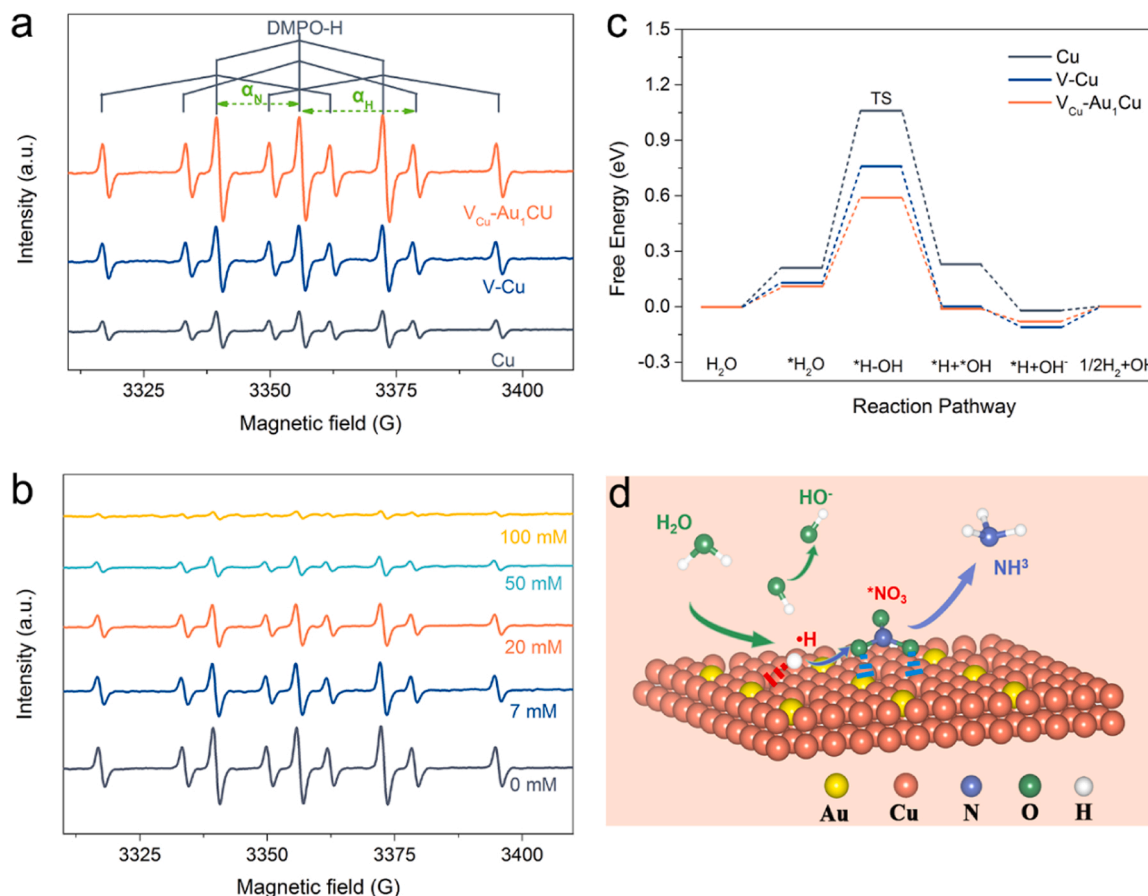


Fig. 4. (a) EPR signals of DMPO spin adducts generated in KOH electrolyte after electrolysis for 5 min by Cu NSs, V-Cu NSs and V_{Cu}-Au₁Cu SAAs at -0.2 V vs. RHE. (b) EPR signals of DMPO spin adducts generated in KOH electrolyte containing different concentrations of KNO₃ after electrolysis by V_{Cu}-Au₁Cu SAAs. (c) Free energy diagrams of H₂O dissociation on Cu NSs (111), V-Cu NSs (111) and V_{Cu}-Au₁Cu SAAs (111) surfaces. (d) Schematic illustration of the reaction mechanism for NITRR on the V_{Cu}-Au₁Cu SAAs surface.

(111), and V_{Cu}-Au₁Cu SAAs (111) surfaces are displayed in Figs. S32 and S34. First, the charge density difference of *NO₃ adsorbed on the surface of the three catalysts was used to investigate the activation of NO₃⁻ (Fig. 5a-c). Bader charge analysis reveals that the adsorbed *NO₃ on Cu NSs (111), V-Cu NSs (111), and V_{Cu}-Au₁Cu SAAs (111) can gain 0.70 e, 0.99 e, and 0.83 e, respectively, suggesting the transfer of electrons from the catalysts to *NO₃, which is thus negatively charged and activated [68]. Fig. 5d shows the Gibbs free energy diagrams of the NITRR to NH₃ on the catalyst surface. For the case of Cu NSs, it was found that there were two uphill steps. The first is the *NO₃ adsorption with a potential barrier of 0.28 eV. The second uphill step is the desorption of *NH₃ from the Cu NSs (111) surface with a potential barrier of 0.54 eV, which is considered the potential-dependent step (PDS). Combined with the tiny free energy of -0.05 eV for *H dimerization to H₂ on Cu NSs (Fig. 4c), its activity and selectivity for NITRR are poor. There is only one uphill step on the V-Cu NSs surface with a smaller potential barrier of 0.15 eV for *NH₃ to desorb to free NH₃, thus leading to a better NITRR performance than Cu NSs. When the V_{Cu}-Au₁Cu SAAs forms, the free energy was decreased gradually with the progress of the NITRR, indicating that the deoxidation and hydrogenation steps on the V_{Cu}-Au₁Cu SAAs are thermodynamically favorable. In addition, the V_{Cu}-Au₁Cu SAAs showed a lower formation energy of *H from H₂O dissociation (Fig. 4c), therefore, the generated *H can easily participate in the NITRR process instead of polymerizing into H₂, enabling V_{Cu}-Au₁Cu SAAs to show the best NITRR activity and selectivity. In total, characterizations combined with theoretical studies evidence that electron migration from Cu to Au atoms creates electron-deficient Cu active sites in V_{Cu}-Au₁Cu SAAs, and the well-defined Cu active sites promote the activation of water to active *H

to boost nitrate hydrogenation and facilitate the desorption of *NH₃, thereby notably promoting intrinsic activity.

3.4. Electrocatalytic NITRR coupled with NH₃ recovery

To obtain the value-added fertilizer, the process of recovering NH₃ from electrolyte was considered to realize the economic route of NO₃⁻ transformation. Among many NH₃ recovery processes, electrochemical gas-permeable membrane process is an attractive technology [69]. As shown in Fig. 6a, a hydrophobic gas membrane was placed between the cathode chamber and the acid chamber. In the cathode chamber, NO₃⁻ is efficiently reduced to NH₃. During the cathodic reaction, the pH of the solution increases. In addition, the electrolyte solution is also alkaline, so its pH value is greater than pK_a (9.3). The generated NH₃ will be spontaneously converted into volatile NH₃, which can subsequently cross over the hydrophobic gas membrane and be recovered by sulfuric acid solution. Therefore, electrochemical reduction nitrate coupled ammonia recovery system was established (Text S3 and Fig. S35) to evaluate the efficiency of nitrogen recovery from NO₃⁻. Fig. 6b shows the variation of nitrogen component concentration in cathode chamber and acid (recovery) chamber with reaction time in continuous-flow at -0.2 V vs. RHE. It was found that nearly 98.8% NO₃⁻ was reduced to NH₃ after 240 min. Meanwhile, approximately 97% NH₃ was recovered in the form of ammonium sulfate. These indicate that electrochemical reduction coupled gas-stripping membrane technology will be an efficient method to recover NH₃ from NO₃⁻ wastewater.

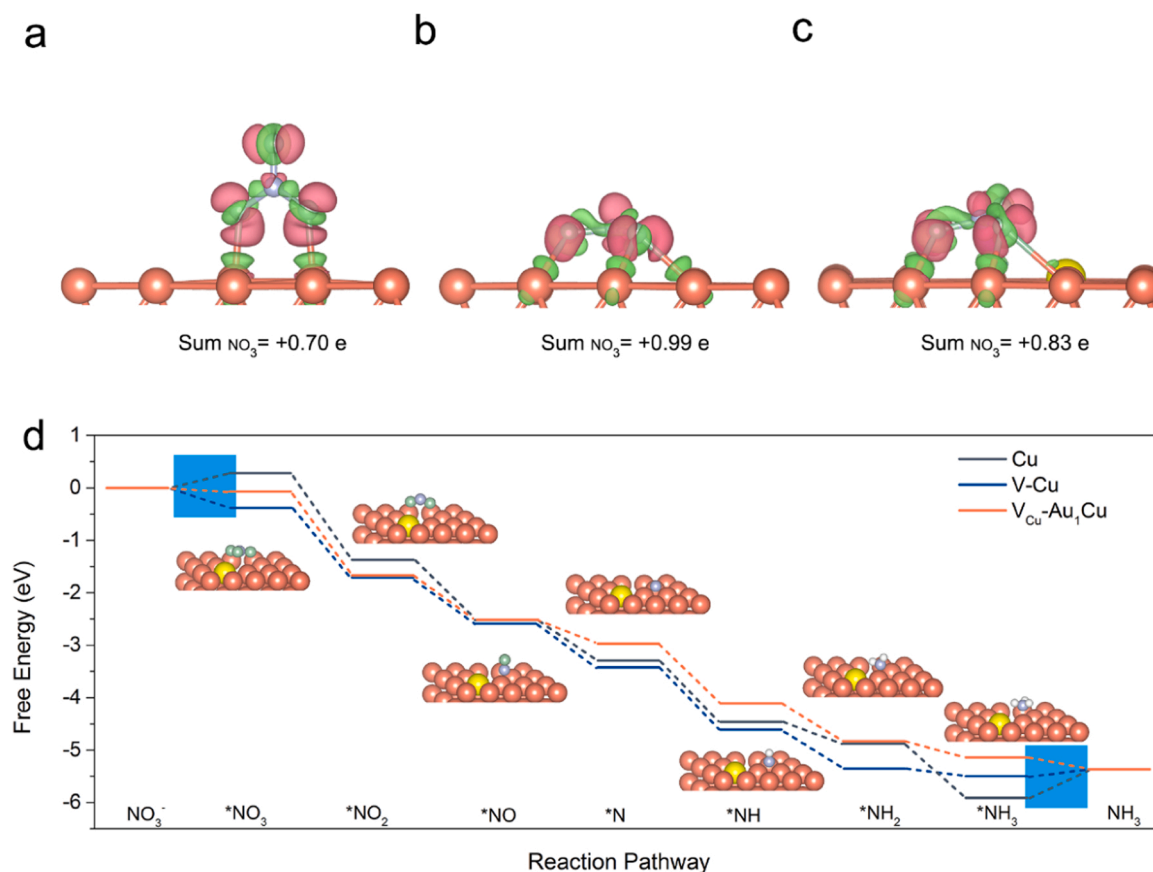


Fig. 5. Charge density difference of $^*\text{NO}_3$ on Cu NSs (a), V-Cu NSs (b) and $\text{V}_{\text{Cu}}\text{-Au}_1\text{Cu}$ SAAs (c). The isosurfaces value is $0.005 \text{ e } \text{\AA}^{-3}$. Pink: charge accumulation, green: charge depletion. (d) Free energy diagrams for the NITRR to NH_3 on Cu NSs (111), V-Cu NSs (111) and $\text{V}_{\text{Cu}}\text{-Au}_1\text{Cu}$ SAAs (111) surfaces. Note that the optimized configurations of intermediates on the $\text{V}_{\text{Cu}}\text{-Au}_1\text{Cu}$ SAA (111) surface are shown.

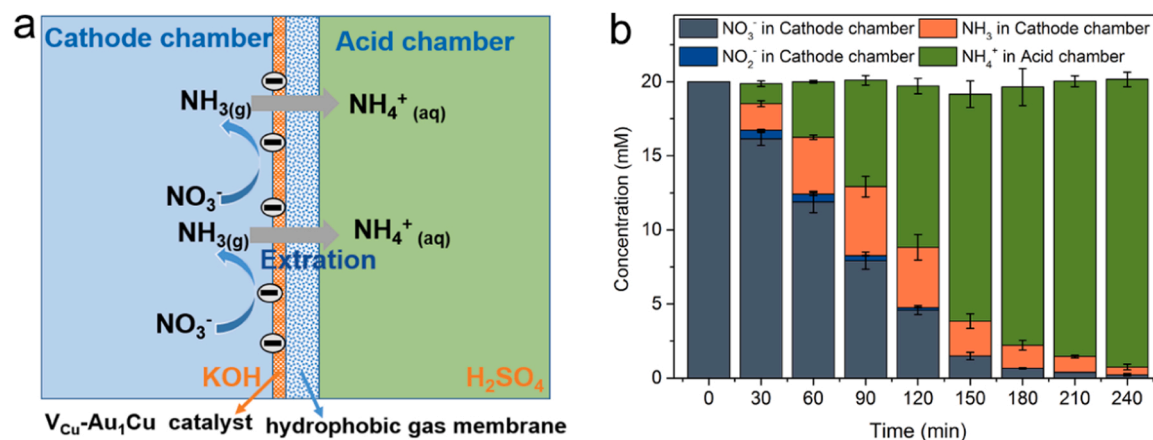


Fig. 6. (a) Schematic diagram of membrane extraction for NH_3 recovery, (b) Time-course changes of components in cathode chamber and acid chamber.

4. Conclusions

In summary, $\text{V}_{\text{Cu}}\text{-Au}_1\text{Cu}$ SAAs were constructed via a facile galvanic replacement with a subsequent dealloying process, which exhibits substantially enhanced activity for NO_3^- electroreduction to NH_3 . The results demonstrate that the isolated Au atoms and adjacent Cu vacancies synergistically regulate the local electronic and geometric structure on the catalytic surface and thus optimize the energetics of intermediate binding. Experiments and theoretical analysis elucidate that the $\text{V}_{\text{Cu}}\text{-Au}_1\text{Cu}$ SAAs structure promotes the activation of H_2O to $^*\text{H}$ to boost

NO_3^- hydrogenation kinetics and facilitates the desorption of $^*\text{NH}_3$, thereby notably promoting intrinsic activity. Our work shows that the local structural environment of the catalyst can be tuned by the synergistic effect of hetero single atoms and surface defects and thus manipulate the catalytic performance. This insight contributes to a fundamental understanding of the exceptional catalytic performance is therefore of providing a guiding design avenue for improving catalysts.

CRediT authorship contribution statement

Yuanzheng Zhang: Conceptualization, Formal analysis, Investigation, Data curation, Writing – original draft. **Xiang Chen:** Validation, Formal analysis, Investigation. **Weilai Wang:** Formal analysis, Visualization. **Lifeng Yin:** Conceptualization, Resources, Data curation, Writing – review & editing, Funding acquisition. **John C. Crittenden:** Writing – review & editing.

Declaration of Competing Interest

The authors declare that they have no known competing financial interests or personal relationships that could have appeared to influence the work reported in this paper.

Acknowledgments

This work was funded partly by the National Natural Science Foundation of China (Grant 21777009), the Bill and Melinda Gates Foundation (INV-003227), Beijing Natural Science Foundation (Grant 8182031).

Appendix A. Supplementary material

Supplementary data associated with this article can be found in the online version at [doi:10.1016/j.apcatb.2022.121346](https://doi.org/10.1016/j.apcatb.2022.121346).

References

- [1] B.H. Suryanto, K. Matuszek, J. Choi, R.Y. Hodgetts, H.-L. Du, J.M. Bakker, C. S. Kang, P.V. Cherepanov, A.N. Simonov, D.R. MacFarlane, Nitrogen reduction to ammonia at high efficiency and rates based on a phosphonium proton shuttle, *Science* 372 (2021) 1187–1191.
- [2] S.Z. Andersen, V. Colić, S. Yang, J.A. Schwalbe, A.C. Nielander, J.M. McEnaney, K. Enemark-Rasmussen, J.G. Baker, A.R. Singh, B.A. Rohr, M.J. Statt, S.J. Blair, S. Mezzavilla, J. Kibsgaard, P.C.K. Vesborg, M. Cargnello, S.F. Bent, T.F. Jaramillo, I.E.L. Stephens, J.K. Nørskov, I. Chorkendorff, A rigorous electrochemical ammonia synthesis protocol with quantitative isotope measurements, *Nature* 570 (2019) 504–508.
- [3] S.L. Foster, S.I.P. Bakovic, R.D. Duda, S. Maheshwari, R.D. Milton, S.D. Minter, M. J. Janik, J.N. Renner, L.F. Greenlee, Catalysts for nitrogen reduction to ammonia, *Nat. Catal.* 1 (2018) 490–500.
- [4] R. Hawtof, S. Ghosh, E. Guarr, C. Xu, R.M. Sankaran, J.N. Renner, Catalyst-free, highly selective synthesis of ammonia from nitrogen and water by a plasma electrolytic system, *Sci. Adv.* 5 (2019) eaat5778.
- [5] S. Garcia-Segura, M. Lanzarini-Lopes, K. Hristovski, P. Westerhoff, Electrocatalytic reduction of nitrate: fundamentals to full-scale water treatment applications, *Appl. Catal. B Environ.* 236 (2018) 546–568.
- [6] B.H. Suryanto, H.-L. Du, D. Wang, J. Chen, A.N. Simonov, D.R. MacFarlane, Challenges and prospects in the catalysis of electroreduction of nitrogen to ammonia, *Nat. Catal.* 2 (2019) 290–296.
- [7] R. Jia, Y. Wang, C. Wang, Y. Ling, Y. Yu, B. Zhang, Boosting selective nitrate electroreduction to ammonium by constructing oxygen vacancies in TiO₂, *ACS Catal.* 10 (2020) 3533–3540.
- [8] Z. Gong, W. Zhong, Z. He, Q. Liu, H. Chen, D. Zhou, N. Zhang, X. Kang, Y. Chen, Regulating surface oxygen species on copper (I) oxides via plasma treatment for effective reduction of nitrate to ammonia, *Appl. Catal. B Environ.* 305 (2022), 121021.
- [9] V. Rosca, M. Duca, M.T. de Groot, M.T. Koper, Nitrogen cycle electrocatalysis, *Chem. Rev.* 109 (2009) 2209–2244.
- [10] R. Daiyan, T. Tran-Phu, P. Kumar, K. Iputera, Z. Tong, J. Leverett, M.H.A. Khan, A. Asghar Esmailpour, A. Jalili, M. Lim, A. Tricoli, R.-S. Liu, X. Lu, E. Lovell, R. Amal, Nitrate reduction to ammonium: from CuO defect engineering to waste NO_x-to-NH₃ economic feasibility, *Energy Environ. Sci.* 14 (2021) 3588–3598.
- [11] J.F. Su, W.-F. Kuan, H. Liu, C.P. Huang, Mode of electrochemical deposition on the structure and morphology of bimetallic electrodes and its effect on nitrate reduction toward nitrogen selectivity, *Appl. Catal. B Environ.* 257 (2019), 117909.
- [12] J.-X. Liu, D. Richards, N. Singh, B.R. Goldsmith, Activity and selectivity trends in electrocatalytic nitrate reduction on transition metals, *ACS Catal.* 9 (2019) 7052–7064.
- [13] Y. Wang, W. Zhou, R. Jia, Y. Yu, B. Zhang, Unveiling the activity origin of a copper-based electrocatalyst for selective nitrate reduction to ammonia, *Angew. Chem. Int. Ed.* 59 (2020) 5350–5354.
- [14] G.A. Cerrón-Calle, A.S. Fajardo, C.M. Sánchez-Sánchez, S. Garcia-Segura, Highly reactive Cu-Pt bimetallic 3D-electrocatalyst for selective nitrate reduction to ammonia, *Appl. Catal. B Environ.* 302 (2021), 120844.
- [15] J. Li, G. Zhan, J. Yang, F. Quan, C. Mao, Y. Liu, B. Wang, F. Lei, L. Li, A.W.M. Chan, L. Xu, Y. Shi, Y. Du, W. Hao, P.K. Wong, J. Wang, S.X. Dou, L. Zhang, J.C. Yu, Efficient ammonia electrosynthesis from nitrate on strained ruthenium nanoclusters, *J. Am. Chem. Soc.* 142 (2020) 7036–7046.
- [16] Y. Wang, A. Xu, Z. Wang, L. Huang, J. Li, F. Li, J. Wicks, M. Luo, D.H. Nam, C. S. Tan, Y. Ding, J. Wu, Y. Lum, C.T. Dinh, D. Sinton, G. Zheng, E.H. Sargent, Enhanced nitrate-to-ammonia activity on copper-nickel alloys via tuning of intermediate adsorption, *J. Am. Chem. Soc.* 142 (2020) 5702–5708.
- [17] Z.Y. Wu, M. Karamad, X. Yong, Q. Huang, D.A. Cullen, P. Zhu, C. Xia, Q. Xiao, M. Shakouri, F.Y. Chen, J.Y.T. Kim, Y. Xia, K. Heck, Y. Hu, M.S. Wong, Q. Li, I. Gates, S. Siahrostami, H. Wang, Electrochemical ammonia synthesis via nitrate reduction on Fe single atom catalyst, *Nat. Commun.* 12 (2021) 2870.
- [18] S. Ye, Z. Chen, G. Zhang, W. Chen, C. Peng, X. Yang, L. Zheng, Y. Li, X. Ren, H. Cao, D. Xue, J. Qiu, Q. Zhang, J. Liu, Elucidating the activity, mechanism and application of selective electrosynthesis of ammonia from nitrate on cobalt phosphide, *Energy Environ. Sci.* 15 (2022) 760–770.
- [19] Y. Guo, R. Zhang, S. Zhang, Y. Zhao, Q. Yang, Z. Huang, B. Dong, C. Zhi, Pd doping-weakened intermediate adsorption to promote electrocatalytic nitrate reduction on TiO₂ nanorods for ammonia production and energy supply with zinc-nitrate batteries, *Energy Environ. Sci.* 14 (2021) 3938–3944.
- [20] Y. Xu, K. Ren, T. Ren, M. Wang, Z. Wang, X. Li, L. Wang, H. Wang, Ultralow-content Pd in-situ incorporation mediated hierarchical defects in corner-etched Cu₂O octahedra for enhanced electrocatalytic nitrate reduction to ammonia, *Appl. Catal. B Environ.* 306 (2022), 121094.
- [21] X. Zhao, X. Li, H. Zhang, X. Chen, J. Xu, J. Yang, H. Zhang, G. Hu, Atomic-dispersed copper simultaneously achieve high-efficiency removal and high-value-added conversion to ammonia of nitrate in sewage, *J. Hazard. Mater.* 424 (2022), 127319.
- [22] S. Zhang, M. Li, J. Li, Q. Song, X. Liu, High-ammonia selective metal-organic framework-derived Co-doped Fe/Fe₂O₃ catalysts for electrochemical nitrate reduction, *Proc. Natl. Acad. Sci. USA* 119 (2022), e2115504119.
- [23] Y.Y. Birdja, E. Pérez-Gallent, M.C. Figueiredo, A.J. Göttle, F. Calle-Vallejo, M.T. M. Koper, Advances and challenges in understanding the electrocatalytic conversion of carbon dioxide to fuels, *Nat. Energy* 4 (2019) 732–745.
- [24] S.-E. Bae, K.L. Stewart, A.A. Gewirth, Nitrate adsorption and reduction on Cu(100) in acidic solution, *J. Am. Chem. Soc.* 129 (2007) 10171–10180.
- [25] X. Wang, P. Ou, J. Wicks, Y. Xie, Y. Wang, J. Li, J. Tam, D. Ren, J.Y. Howe, Z. Wang, A. Ozden, Y.Z. Finckel, Y. Xu, Y. Li, A.S. Rasouli, K. Bertens, A.H. Ip, M. Graetzel, D. Sinton, E.H. Sargent, Gold-in-copper at low *CO coverage enables efficient electromethanation of CO₂, *Nat. Commun.* 12 (2021) 3387.
- [26] A. Wang, J. Li, T. Zhang, Heterogeneous single-atom catalysis, *Nat. Rev. Chem.* 2 (2018) 65–81.
- [27] R.T. Hannagan, G. Giannakakis, M. Flytzani-Stephanopoulos, E.C.H. Sykes, Single-atom alloy catalysis, *Chem. Rev.* 120 (2020) 12044–12088.
- [28] H. Feng, J. Yu, L. Tang, J. Wang, H. Dong, T. Ni, J. Tang, W. Tang, X. Zhu, C. Liang, Improved hydrogen evolution activity of layered double hydroxide by optimizing the electronic structure, *Appl. Catal. B Environ.* 297 (2021), 120478.
- [29] N. Guo, H. Xue, A. Bao, Z. Wang, J. Sun, T. Song, X. Ge, W. Zhang, K. Huang, F. He, Q. Wang, Achieving superior electrocatalytic performance by surface copper vacancy defects during electrochemical etching process, *Angew. Chem. Int. Ed.* 59 (2020) 13778–13784.
- [30] W. Luc, X. Fu, J. Shi, J.-J. Lv, M. Jouny, B.H. Ko, Y. Xu, Q. Tu, X. Hu, J. Wu, Q. Yue, Y. Liu, F. Jiao, Y. Kang, Two-dimensional copper nanosheets for electrochemical reduction of carbon monoxide to acetate, *Nat. Catal.* 2 (2019) 423–430.
- [31] X. Fu, X. Zhao, X. Hu, K. He, Y. Yu, T. Li, Q. Tu, X. Qian, Q. Yue, M.R. Wasielewski, Y. Kang, Alternative route for electrochemical ammonia synthesis by reduction of nitrate on copper nanosheets, *Appl. Mater. Today* 19 (2020), 100620.
- [32] M.B. Boucher, B. Zugic, G. Cladaras, J. Kammert, M.D. Marcinkowski, T.J. Lawton, E.C. Sykes, M. Flytzani-Stephanopoulos, Single atom alloy surface analogs in Pd_{0.18}Cu_{0.82} nanoparticles for selective hydrogenation reactions, *Phys. Chem. Chem. Phys.* 15 (2013) 12187–12196.
- [33] H. Zhang, T. Watanabe, M. Okumura, M. Haruta, N. Toshima, Catalytically highly active top gold atom on palladium nanocluster, *Nat. Mater.* 11 (2012) 49–52.
- [34] G.W. Watt, J.D. Chrisp, Spectrophotometric method for determination of hydrazine, *Anal. Chem.* 24 (1952) 2006–2008.
- [35] G. Kresse, J. Furthmüller, Efficient iterative schemes for ab initio total-energy calculations using a plane-wave basis set, *Phys. Rev. B* 54 (1996) 11169–11186.
- [36] G. Kresse, J. Furthmüller, Efficiency of ab-initio total energy calculations for metals and semiconductors using a plane-wave basis set, *Comput. Mater. Sci.* 6 (1996) 15–50.
- [37] J.P. Perdew, K. Burke, M. Ernzerhof, Generalized gradient approximation made simple, *Phys. Rev. Lett.* 77 (1996) 3865–3868.
- [38] L. Jiang, K. Liu, S.F. Hung, L. Zhou, N. Zheng, Facet engineering accelerates spillover hydrogenation on highly diluted metal nanocatalysts, *Nat. Nanotechnol.* 15 (2020) 848–853.
- [39] W. Zhang, C. Huang, Q. Xiao, L. Yu, L. Shuai, P. An, J. Zhang, M. Qiu, Z. Ren, Y. Yu, Atypical oxygen-bearing copper boosts ethylene selectivity toward electrocatalytic CO₂ reduction, *J. Am. Chem. Soc.* 142 (2020) 11417–11427.
- [40] D. Cao, H. Xu, D. Cheng, Construction of defect-rich RhCu nanotubes with highly active Rh₃Cu₁ alloy phase for overall water splitting in all pH values, *Adv. Energy Mater.* 10 (2020), 1903038.
- [41] G.L. De Gregorio, T. Burdyny, A. Loiudice, P. Iyengar, W.A. Smith, R. Buonsanti, Facet-dependent selectivity of Cu catalysts in electrochemical CO₂ reduction at commercially viable current densities, *ACS Catal.* 10 (2020) 4854–4862.
- [42] R. Long, Y. Li, Y. Liu, S. Chen, X. Zheng, C. Gao, C. He, N. Chen, Z. Qi, L. Song, J. Jiang, J. Zhu, Y. Xiong, Isolation of Cu atoms in Pd lattice: forming highly

- selective sites for photocatalytic conversion of CO₂ to CH₄, *J. Am. Chem. Soc.* 139 (2017) 4486–4492.
- [43] Z. Zhang, G. Wen, D. Luo, B. Ren, Y. Zhu, R. Gao, H. Dou, G. Sun, M. Feng, Z. Bai, A. Yu, Z. Chen, “Two ships in a bottle” design for Zn-Ag-O catalyst enabling selective and long-lasting CO₂ electroreduction, *J. Am. Chem. Soc.* 143 (2021) 6855–6864.
- [44] J.Y. Park, L.R. Baker, G.A. Somorjai, Role of hot electrons and metal-oxide interfaces in surface chemistry and catalytic reactions, *Chem. Rev.* 115 (2015) 2781–2817.
- [45] R. Si, M. Flytzani-Stephanopoulos, Shape and crystal-plane effects of nanoscale ceria on the activity of Au-CeO₂ catalysts for the water-gas shift reaction, *Angew. Chem. Int. Ed.* 47 (2008) 2884–2887.
- [46] I. Najdovski, P.R. Selvakannan, S.K. Bhargava, A.P. O'Mullane, Formation of nanostructured porous Cu-Au surfaces: the influence of cationic sites on (electro)-catalysis, *Nanoscale* 4 (2012) 6298.
- [47] D. Kim, C. Xie, N. Becknell, Y. Yu, M. Karamad, K. Chan, E.J. Crumlin, J. K. Norskov, P. Yang, Electrochemical Activation of CO₂ through atomic ordering transformations of AuCu nanoparticles, *J. Am. Chem. Soc.* 139 (2017) 8329–8336.
- [48] L. Jiang, K. Liu, S.F. Hung, L. Zhou, R. Qin, Q. Zhang, P. Liu, L. Gu, H.M. Chen, G. Fu, N. Zheng, Facet engineering accelerates spillover hydrogenation on highly diluted metal nanocatalysts, *Nat. Nanotechnol.* 15 (2020) 848–853.
- [49] X. Zhang, S. Han, B. Zhu, G. Zhang, X. Li, Y. Gao, Z. Wu, B. Yang, Y. Liu, W. Baaziz, O. Ersen, M. Gu, J.T. Miller, W. Liu, Reversible loss of core-shell structure for Ni-Au bimetallic nanoparticles during CO₂ hydrogenation, *Nat. Catal.* 3 (2020) 411–417.
- [50] M. Mihaylov, H. Knözinger, K. Hadjiivanov, B.C. Gates, Characterization of the oxidation states of supported gold species by IR spectroscopy of adsorbed CO, *Chem. Ing. Tech.* 79 (2007) 795–806.
- [51] M. Ouyang, K.G. Papanikolaou, A. Boubnov, A.S. Hoffman, G. Giannakakis, S. R. Bare, M. Stamatakis, M. Flytzani-Stephanopoulos, E.C.H. Sykes, Directing reaction pathways via in situ control of active site geometries in PdAu single-atom alloy catalysts, *Nat. Commun.* 12 (2021) 1549.
- [52] X. Zhang, G. Cui, H. Feng, L. Chen, H. Wang, B. Wang, X. Zhang, L. Zheng, S. Hong, M. Wei, Platinum-copper single atom alloy catalysts with high performance towards glycerol hydrogenolysis, *Nat. Commun.* 10 (2019) 1–12.
- [53] D. Kim, J. Resasco, Y. Yu, A.M. Asiri, P. Yang, Synergistic geometric and electronic effects for electrochemical reduction of carbon dioxide using gold-copper bimetallic nanoparticles, *Nat. Commun.* 5 (2014) 4948.
- [54] M. Liu, Y. Pang, B. Zhang, P. De Luna, O. Voznyy, J. Xu, X. Zheng, C.T. Dinh, F. Fan, C. Cao, F.P. de Arquer, T.S. Safaei, A. Mephram, A. Klinkova, E. Kumacheva, T. Filleter, D. Sinton, S.O. Kelley, E.H. Sargent, Enhanced electrocatalytic CO₂ reduction via field-induced reagent concentration, *Nature* 537 (2016) 382–386.
- [55] Y. Yang, Y. Qian, H. Li, Z. Zhang, Y. Mu, D. Do, B. Zhou, J. Dong, W. Yan, Y. Qin, O-coordinated W-Mo dual-atom catalyst for pH-universal electrocatalytic hydrogen evolution, *Sci. Adv.* 6 (2020) eaba6586.
- [56] H. Liu, J. Park, Y. Chen, Y. Qiu, Y. Cheng, K. Srivastava, S. Gu, B.H. Shanks, L. T. Roling, W. Li, Electrocatalytic nitrate reduction on oxide-derived silver with tunable selectivity to nitrite and ammonia, *ACS Catal.* 11 (2021) 8431–8442.
- [57] Y. Zhang, X. Chen, S. Zhang, L. Yin, Y. Yang, Defective titanium dioxide nanobamboo arrays architecture for photocatalytic nitrogen fixation up to 780 nm, *Chem. Eng. J.* 401 (2020), 126033.
- [58] V.R. Stamenkovic, B. Fowler, B.S. Mun, G. Wang, P.N. Ross, C.A. Lucas, N. M. Marković, Improved oxygen reduction activity on Pt₃Ni (111) via increased surface site availability, *Science* 315 (2007) 493–497.
- [59] J.G. Chen, R.M. Crooks, L.C. Seefeldt, K.L. Bren, R.M. Bullock, M.Y. Darensbourg, P.L. Holland, B. Hoffman, M.J. Janik, A.K. Jones, M.G. Kanatzidis, P. King, K. M. Lancaster, S.V. Lyman, P. Pfomm, W.F. Schneider, R.R. Schrock, Beyond fossil fuel-driven nitrogen transformations, *Science* 360 (2018) eaar6611.
- [60] M.C.O. Monteiro, A. Goyal, P. Moerland, M.T.M. Koper, Understanding cation trends for hydrogen evolution on platinum and gold electrodes in alkaline media, *ACS Catal.* 11 (2021) 14328–14335.
- [61] Y. Zhang, Y. Dai, H. Li, L. Yin, M.R. Hoffmann, Proton-assisted electron transfer and hydrogen-atom diffusion in a model system for photocatalytic hydrogen production, *Commun. Mater.* 1 (2020) 1–9.
- [62] G.-F. Chen, Y. Yuan, H. Jiang, S.-Y. Ren, L.-X. Ding, L. Ma, T. Wu, J. Lu, H. Wang, Electrochemical reduction of nitrate to ammonia via direct eight-electron transfer using a copper-molecular solid catalyst, *Nat. Energy* 5 (2020) 605–613.
- [63] Y. Zheng, Y. Jiao, Y. Zhu, L.H. Li, Y. Han, Y. Chen, M. Jaroniec, S.-Z. Qiao, High electrocatalytic hydrogen evolution activity of an anomalous ruthenium catalyst, *J. Am. Chem. Soc.* 138 (2016) 16174–16181.
- [64] C.-T. Dinh, A. Jain, F.P.G. de Arquer, P. De Luna, J. Li, N. Wang, X. Zheng, J. Cai, B. Z. Gregory, O. Voznyy, B. Zhang, M. Liu, D. Sinton, E.J. Crumlin, E.H. Sargent, Multi-site electrocatalysts for hydrogen evolution in neutral media by destabilization of water molecules, *Nat. Energy* 4 (2019) 107–114.
- [65] Q. Wu, M. Luo, J. Han, W. Peng, Y. Zhao, D. Chen, M. Peng, J. Liu, F.M.F. de Groot, Y. Tan, Identifying electrocatalytic sites of the nanoporous copper-ruthenium alloy for hydrogen evolution reaction in alkaline electrolyte, *ACS Energy Lett.* 5 (2019) 192–199.
- [66] F. Cai, Y. Guo, J.J. Ibrahim, J. Zhang, Y. Sun, A highly active and stable Pd/MoC catalyst for hydrogen production from methanol decomposition, *Appl. Catal. B Environ.* 299 (2021), 120648.
- [67] E. Liu, L. Jiao, J. Li, T. Stracensky, Q. Sun, S. Mukerjee, Q. Jia, Interfacial water shuffling the intermediates of hydrogen oxidation and evolution reactions in aqueous media, *Energy Environ. Sci.* 13 (2020) 3064–3074.
- [68] J. Wang, X. Huang, S. Xi, H. Xu, X. Wang, Axial modification of cobalt complexes on heterogeneous surface with enhanced electron transfer for carbon dioxide reduction, *Angew. Chem. Int. Ed.* 59 (2020) 19162–19167.
- [69] C. Zhang, J. Ma, J. Song, C. He, T.D. Waite, Continuous ammonia recovery from wastewaters using an integrated capacitive flow electrode membrane stripping system, *Environ. Sci. Technol.* 52 (2018) 14275–14285.